Modeling of the Effects of Surface-Active Elements on Flow Patterns and Weld Penetration

Y. WANG, Q. SHI, and H.L. TSAI

A mathematical model was developed to calculate the transient temperature and velocity distributions in a stationary gas tungsten arc (GTA) weld pool of 304 stainless steels with different sulfur concentrations. A parametric study showed that, depending upon the sulfur concentration, one, two, or three vortexes may be found in the weld pool. These vortexes are caused by the interaction between the electromagnetic force and surface tension, which is a function of temperature and sulfur concentration, and have a significant effect on weld penetration. For given welding conditions, a minimum threshold sulfur concentration is required to create a single, clockwise vortex for deep penetration. When two metals with different sulfur concentrations are welded together, the weld-pool shape is skewed toward the metal with a lower sulfur content. Detailed physical insights on complicated fluid-flow phenomena and the resulting weld-pool penetration were obtained, based on the surface tension–temperature–sulfur concentration relationships.

I. INTRODUCTION

THE effect of trace elements on weld penetration was discovered long ago. Oyler *et al.*[1] reported that some heats of vacuum-arc–remelted type 304 L stainless steel were "troublesome" to weld. They found that a balance of the chemical composition of all elements must be maintained to guarantee good weldability. However, although they attributed the inconsistent weld penetration to the composition of the steels, the effect of the trace elements on surface tension and the resulting fluid flow in the weld pool, leading to the variation of weld penetration, was not fully understood.

Perhaps, Heiple and co-workers[2–7] were the first to systematically study the phenomenon of surface-active elements in the weld pool in early 1980s. In their first article,[2] Heiple *et al.* found that with the change of aluminum concentration in austenitic stainless steel, the depth/width ratio of weldments can be reduced in gas tungsten arc (GTA) welds. Later, they observed that small additions of selenium to stainless steel dramatically increased the depth/width ratio of the weld.[3] The effects of other surface-active elements (S, O, Te, and Ce) on weld shape in 21-6-9 stainless steels were also studied.[4] Based on the experimental results, Heiple *et al.*[5,6] proposed that surface tension–driven fluid flow is responsible, in many cases, for the fluid-flow patterns in the weld pool, and that trace elements change fluid-flow patterns by altering the surface-tension gradient. Several flow patterns have been proposed to explain the effect of surface tension on flow patterns and the resulting weld penetration. In their studies, Heiple and Burgardt[7] found that small additions of SO_2 in argon gas for GTA welding both suppressed variability and improved joint penetration in 21-6-9 and 304 stainless steels. However, as it is very difficult to measure in real time the fluid flow in the weld pool, validation of the surface-tension effect has been limited to the metallographic characterization of the solidified weld-pool shape and measurement of the surface temperature of the weld pool.

Since the middle of the 1980s, many theoretical models have been proposed to study the effect of surface tension on weld-pool fluid flow and penetration. These include Kou and co-workers,[8,9,10] Zacharia and co-workers,[11–14] Szekely and co-workers,[15–19] and others.[20,21] Kou and Wang[8] and Tsai and Kou[10] were able to predict a reverse flow phenomenon by changing the sign of the surface-tension temperature gradient ($\partial\gamma/\partial T$) from a negative value to a positive one. Also, in their two-dimensional calculation, Kou and Sun[9] calculated the weld-pool shape in a steady-state GTA spot weld and considered three driving forces for the fluid flow: buoyancy force, electromagnetic force, and surface tension at the weld-pool surface. In their earlier work, Zacharia *et al.*[11] developed a model to realistically simulate the transient, multidimensional heat-transfer and flow conditions throughout the period of a typical welding process. Later, Zacharia *et al.*[12] developed a multidimensional mathematical model to simulate the convection and heat transfer of a GTA weld pool by considering $\partial\gamma/\partial T$ as a function of temperature and sulfur concentration. Their modeling results were validated by experimental measurements. Zacharia *et al.*[13] developed a transient multidimensional model to investigate coupled conduction and convection heat-transfer problems associated with stationary and moving arc-welding situations.

The effect of evaporation and temperature-dependent material properties on weld-pool development was also studied by Zacharia *et al.*[14] After studying the influence of surface-active elements on the surface velocities and weld-pool shape in the welding process, Oreper and Szekely[15] found that both the convective-flow field and temperature field were remarkably affected by the nature of the heat flux and the flux of electric current falling on the free surface. The transient heat transfer and fluid flow in the weld pool with a deformed free surface were modeled using a two-dimensional coordinate transformation by Thompson and Szekely.[16] From the results of the study by Choo *et al.*,[17]

Y. WANG and Q. SHI, Graduate Students, and H.L. TSAI, Professor of Mechanical Engineering, are with the Department of Mechanical and Aerospace Engineering and Engineering Mechanics, University of Missouri–Rolla, Rolla, MO 65409.

Manuscript submitted January 10, 1997.

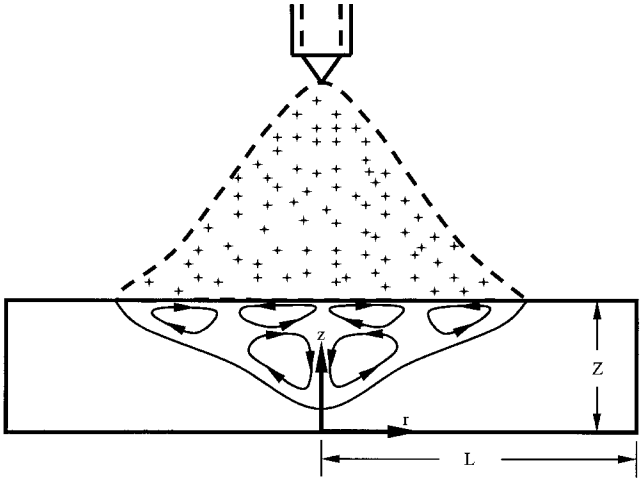

Fig. 1—Schematic sketch of a stationary GTAW system and dimensions of the welding workpiece.

it was concluded that the flow patterns in deformed weld pools may be more complex than previously thought. Choo and Szekely[18] studied the effect of alloy-element vaporization on weld-pool heat transfer and fluid flow. Choo *et al.*[19] found in their study that the free-surface temperature of the weld pool appears to be limited by Marangoni convection rather than by the heat losses due to vaporization. Kim and Na[20] have also studied the effects of a deformable free surface in the weld pool.

Woods and Milner[21] performed some experiments to study convection in the weld pool by examining the mixing of dissimilar metal droplets in the pool. Keene *et al.*[22] measured the surface tension for the Fe-S-O ternary system and the two binary systems, Fe-O and Fe-S, by using the levitated drop technique. The two articles by Mills and Keene[23] and Burgardt and Campbell[24] gave good reviews on the factors affecting weld penetration. Although it has been observed experimentally[23,24] that a skewed weldment was formed when the two steels with different sulfur contents were welded together, there is no theoretical model predicting this phenomenon.

From the previous review, it can be said that the effects of surface-active elements on fluid flow and weld penetration have been quite well modeled and understood. However, there are several issues still needing to be addressed, including (1) the possible existence of a threshold sulfur concentration in order to achieve full penetration under given welding conditions; (2) the possible existence of several vortexes in the weld pool and how they affect the weld penetration; and (3) the instance when two metals with different contents of surface-active elements are welded together. Hence, the aim of the present study is to provide the solutions to the aforementioned issues.

II. MATHEMATICAL MODEL

A. *Governing Equations*

Figure 1 is a schematic sketch of a stationary GTA weld, with the welding arc in a Gaussian distribution, which provides an incident flux of thermal energy at the top surface of the metal. The metal is heated and melted, and the transient distributions of temperature and metal-flow velocity in the melt are sought by solving the governing partial differential equations. Based on the continuum formulation by Diao and Tsai,[25] the continuity, momentum, and energy equations in the cylindrical coordinate system ($r - z$) are expressed as follows.

Continuity:

$$\frac{\partial}{\partial t}(\rho) + \nabla \cdot (\rho \mathbf{V}) = 0 \qquad [1]$$

Momentum:

$$\frac{\partial}{\partial t}(\rho u) + \nabla \cdot (\rho \mathbf{V} u) = \nabla \cdot \left(\mu_l \frac{\rho}{\rho_l} \nabla u\right) - \frac{\partial p}{\partial r} - \frac{\mu_l}{K}\frac{\rho}{\rho_l}(u - u_s) - \frac{C\rho^2}{K^{1/2}\rho_l}|u - u_s|(u - u_s) - \nabla \cdot (\rho f_s f_l \mathbf{V}_r u_r) - J_z B_\theta \qquad [2]$$

$$\frac{\partial}{\partial t}(\rho v) + \nabla \cdot (\rho \mathbf{V} v) = \nabla \cdot \left(\mu_l \frac{\rho}{\rho_l} \nabla v\right) - \frac{\partial p}{\partial z} - \frac{\mu_l}{K}\frac{\rho}{\rho_l}(v - v_s) - \frac{C\rho^2}{K^{1/2}\rho_l}|v - v_s|(v - v_s) - \nabla \cdot (\rho f_s f_l \mathbf{V}_r v_r) + \rho g(\beta_T(T - T_0) + \beta_s(f_l^\alpha - f_{l,0}^\alpha)) + J_r B_\theta \qquad [3]$$

Energy:

$$\frac{\partial}{\partial t}(\rho h) + \nabla \cdot (\rho \mathbf{V} h) = \nabla \cdot \left(\frac{k}{c_s} \nabla h\right) + \nabla \cdot \left(\frac{k}{c_s} \nabla (h_s - h)\right) - \nabla \cdot (\rho(\mathbf{V} - \mathbf{V}_s)(h_l - h)) \qquad [4]$$

The previous four equations are similar to those given in Reference 25, except that the last term in both Eqs. [2] and [3] represents the electromagnetic force (or Lorentz force) due to the applied welding arc. As the assumptions to derive the equations and the physical meaning of other terms are given by Diao and Tsai,[25] they are not repeated here. The electromagnetic force is assumed to be independent of the fluid flow in the weld pool, and their r and z components are calculated first, as discussed next. The second-from-the-last term in Eq. [3] is based on the Boussinesq approximation for natural convection caused by both temperature and solutal convection. However, the solutal convection will only become effective when two metals with different sulfur concentrations are welded together (as discussed in Section III–F).

In Eqs. [1] through [4], the continuum density, specific heat, thermal conductivity, solid mass fraction, liquid mass fraction, velocity, and enthalpy are defined as follows:

$$\rho = g_s\rho_s + g_l\rho_l;\ c = f_s c_s + f_l c_l;\ k = g_s k_s + g_l k_l$$
$$f_s = \frac{g_s\rho_s}{\rho};\ f_l = \frac{g_l\rho_l}{\rho} \qquad [5]$$
$$\mathbf{V} = f_s\mathbf{V}_s + f_l\mathbf{V}_l;\ h = h_s f_s + h_l f_l$$

where g_s and g_l are the volume fractions of the solid and liquid phases, respectively. If the phase specific heats are assumed to be constant, the phase enthalpy for the solid and liquid can be expressed as

$$h_s = c_s T;\ h_l = c_l T + (c_s - c_l)T_s + H \qquad [6]$$

where H is the latent heat of fusion of the alloy and T_s is the solidus temperature.

The assumption of a permeability function in the mushy zone requires consideration of the growth morphology specific to the alloy under study. In the present study, the permeability function analogous to fluid flow in a porous media is assumed, employing the Carman–Kozeny equation:[25]

$$K = \frac{g_l^3}{c_l(1 - g_l)^2};\ c_l = \frac{180}{d^2} \quad [7]$$

where d is proportional to the dendrite dimension, which is assumed to be a constant and is on the order of 10^{-2} cm. The inertial coefficient (C) can be calculated from[25]

$$C = 0.13\ g_l^{-3/2} \quad [8]$$

In the previous governing differential equations (Eqs. [1] through [4]), there is a solid-phase velocity. The solid-phase velocity is associated with the movement of precipitated solid equiaxed grains and/or broken dendrites in the mushy zone. Certain relations may exist between the solid-phase and liquid-phase velocity; however, the exact relations are not known at this time. For the welding conditions used in the present study, the weld bead and the mushy zone, which is limited to the bottom and the edge of the weld pool, are small compared to the typical solidification of a casting ingot. Hence, the solid-phase velocity is assumed to be zero, and the equations are simplified accordingly. Also, as the solidification time is very short (about 0.3 seconds in the present study) and the mushy zone is small, there is no time for interdendritic fluid flow to develop.[26] Hence, the possible formation of macrosegregation due to the interdendritic flow of solute–rich/poor liquid is ignored.[26] In other words, it is assumed that the nonuniform distribution of sulfur in the weld pool is caused only by the "mixing effect" due to macroscopic convection flow in the liquid phase.

During melting or solidification, a supplementary relation is required to incorporate the latent-heat absorption or release, which is assumed to be proportional to the liquid mass fraction (f_l) or the solid mass fraction ($f_s = 1 - f_l$) in the weld pool. The actual mode of latent-heat release depends upon factors such as the alloy composition as well as the evolution of microstructures and includes recalescence. In the present study, the latent heat is absorbed or released according to the following relation:[27]

$$f_s = \frac{T_l - T}{T_l - T_s} \text{ for } T_s \le T \le T_l \quad [9]$$

where T_l is the liquidus temperature.

B. *Boundary Conditions*

In the present study, the top free surface is assumed to be flat, although the surface can be deformed by the arc force.[10,16] The boundary conditions for Eqs. [1] through [4] are given subsequently.

1. *At the top surface (z = Z)*:

$$k\frac{\partial T}{\partial z} = \frac{\eta I u_w}{2\pi\sigma_q^2}\exp\left(-\frac{r^2}{2\sigma_q^2}\right) - q_{\text{conv}} - q_{\text{radi}} - q_{\text{evap}} \quad [10]$$

$$\mu_l\frac{\partial u}{\partial z} = \frac{\partial\gamma}{\partial T}\frac{\partial T}{\partial r} + \frac{\partial\gamma}{\partial f^\alpha}\frac{\partial f^\alpha}{\partial r};\ v = 0 \quad [11]$$

where I is the welding current, η is the arc heat efficiency, u_w is the arc voltage, and σ_q is the arc heat-flux distribution parameter. The first term in Eq. [10] represents the thermal flux from the welding arc, and the rest of the terms represent the heat losses to the ambient environment through convection, radiation, and liquid-metal vaporization, respectively. Equation [11] represents the shear stress at the top free surface, which can be caused by surface tension (γ) and/or by drag force due to inert gases. The effect of the drag force has been reported to be small;[17,20] hence, it is neglected in the present study. The surface tension is a function of both temperature and concentration of the sulfur (f^α), and its formula will be discussed next. When welding metals have the same content of surface-active elements, the second term on the right-hand side of Eq. [11] is zero. However, if metals with different sulfur concentrations are welded together, this term should be considered (refer to Section III–F). Heat losses from the metal to its surroundings due to convection, radiation, and evaporation can be written as

$$q_{\text{conv}} = h_c(T - T_\infty) \quad [12]$$

$$q_{\text{radi}} = \sigma\varepsilon(T^4 - T_\infty^4) \quad [13]$$

$$q_{\text{evap}} = WH_v \quad [14]$$

where h_c is the convective heat-transfer coefficient between the metal and its surroundings at temperature T_∞, σ is the Stefan–Boltzmann constant, ε is the radiation emissivity, W is the liquid-metal evaporation rate, and H_v is the latent heat for the liquid-vapor phase change. For metals such as steels, W can be written as[14,28]

$$\log W = A_v + \log P_{\text{atm}} - 0.5\log T \quad [15]$$

with

$$\log P_{\text{atm}} = 6.121 - \frac{18{,}836}{T} \quad [16]$$

where A_v is a constant and P_{atm} is the atmospheric pressure.

2. *At the bottom surface (z = 0)*:

$$-k\frac{\partial T}{\partial z} = q_{\text{conv}} \quad [17]$$

$$u = 0;\ v = 0 \quad [18]$$

3. *Along the symmetrical axis (r = 0)*:

$$\frac{\partial T}{\partial r} = 0 \quad [19]$$

$$u = 0;\ \frac{\partial v}{\partial r} = 0 \quad [20]$$

4. *At the outer surface (r = L)*:

$$-k\frac{\partial T}{\partial r} = q_{\text{conv}} \quad [21]$$

$$u = 0;\ v = 0 \quad [22]$$

C. *Electromagnetic Force*

In order to solve Eqs. [2] and [3], the last term caused by the electromagnetic force should be calculated first. Assuming that the electric field is quasisteady-state and the

electrical conductivity is constant, the scalar electric potential (ϕ) satisfies the following Maxwell equation:[19]

$$\nabla^2\phi = \frac{1}{r}\frac{\partial}{\partial r}\left(r\frac{\partial\phi}{\partial r}\right) + \frac{\partial^2\phi}{\partial z^2} = 0 \qquad [23]$$

The required boundary conditions for the solution of Eq. [23] are

$$-\sigma_e\frac{\partial\phi}{\partial z} = \frac{\mathrm{I}}{2\pi\sigma_q^2}\exp\left(-\frac{r^2}{2\sigma_q^2}\right);\ \text{at } z = Z \qquad [24]$$

$$\frac{\partial\phi}{\partial z} = 0;\ \text{at } z = 0 \qquad [25]$$

$$\frac{\partial\phi}{\partial r} = 0;\ \text{at } r = 0 \qquad [26]$$

$$\phi = 0;\ \text{at } r = L \qquad [27]$$

where σ_e is the electrical conductivity. Note that, as the heat-flux energy comes from the welding current, the current distribution parameter (σ_q) in Eq. [24] is chosen to be the same as that in Eq. [10] for the heat flux. However, they can be different. After the distribution of electrical potential is solved, the distributions of current density in the *r* and *z* directions can be calculated *via*

$$J_r = -\sigma_e\frac{\partial\phi}{\partial r} \qquad [28]$$

$$J_z = -\sigma_e\frac{\partial\phi}{\partial z} \qquad [29]$$

The self-induced azimuthal magnetic field is derived from Ampere's law *via*[19]

$$B_\theta = \frac{\mu_0}{r}\int_0^r J_z r\,dr \qquad [30]$$

where μ_0 is the magnetic permeability. Finally, the two components of electromagnetic force in Eqs. [2] and [3] are calculated *via*

$$\mathbf{J}\times\mathbf{B}|_r = -J_z B_\theta \qquad [31]$$

$$\mathbf{J}\times\mathbf{B}|_z = J_r B_\theta \qquad [32]$$

D. *Surface Tension*

The surface tension for a pseudobinary Fe-S system, as a function of temperature and the sulfur concentration, is given by[29]

$$\gamma = 1.943 - 4.3\cdot10^{-4}(T-1723) - \mathrm{R}T\cdot1.3\cdot10^{-8}\ln\left(1+0.00318\,f^{\alpha}\exp\left(\frac{1.66\cdot10^8}{\mathrm{R}T}\right)\right) \qquad [33]$$

where R is the gas constant. The surface tension is plotted in Figure 2 as a function of temperature for several different sulfur concentrations. Three observations can be made in Figure 2: (1) the basic characteristics of the surface tension *vs* temperature curves have been changed due to the addition of sulfur in steels; (2) at the same temperature, the value of the surface tension decreases as the content of sulfur increases; and (3) the temperature at which the maximum surface tension occurs increases as the sulfur concentration increases. A dotted line tracing the maximum surface tension for different sulfur concentrations ($\partial\gamma/\partial T = 0$) is also shown in Figure 2. For a given sulfur concentration, as the temperature increases, the surface tension increases, reaches a maximum value, and then decreases thereafter.

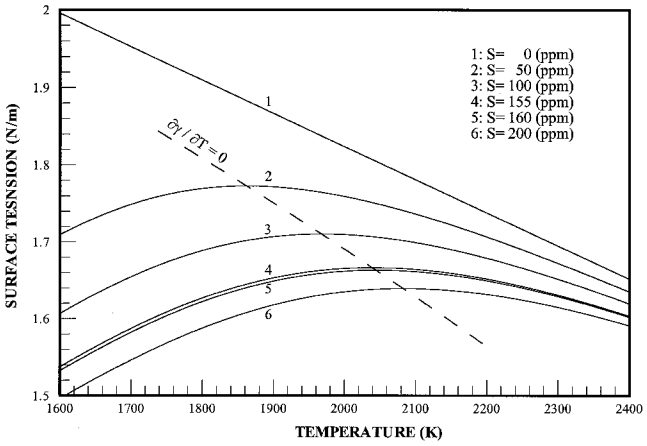

Fig. 2—Surface tension as a function of temperature and sulfur concentration for the pseudobinary Fe-S system. The dotted line traces the points with maximum surface tension for different sulfur concentrations.

E. *Numerical Method*

Prior to solving the coupled continuity, momentum, and energy equations (and also the species equation, as discussed in Section III–F), the two components of electromagnetic force in Eqs. [2] and [3] need to be obtained. This was accomplished by solving Eq. [23] and its associated boundary conditions (Eqs. [24] through [27]) and then by solving Eqs. [28] through [32]. An implicit, control volume–based finite-difference method using the SIMPLEC algorithm was used for the solution of Eqs. [1] through [4].[30] Basically, the numerical method used in the present study is similar to the one used in previous articles;[31,32] hence, it is not to be repeated here.

A fixed-grid system of 50 × 29 grid points was utilized for the welding domain of 15 × 5 mm. A finer grid spacing was used in the weld-pool region because of the higher temperature and velocity gradients. To check the accuracy of the calculated results, a finer grid system was used by reducing the grid spacing to half (*i.e.*, 99 × 57). Although it took about 4 times the central processing unit (CPU) time, as compared to the original grid system, little improvement was found with the finer grid system. As a result, the 50 × 29 grid system was used for all calculations. The selected grid system can be considered to be a compromise between computational cost and accuracy. Calculations were executed on HEWLETT-PACKARD* H-P-9000/735 workstations, and it took about 3 hours of CPU time to perform a typical analysis.

*HEWLETT-PACKARD and H-P are trademarks of the Hewlett-Packard Company, Palo Alto, CA.

III. RESULTS AND DISCUSSION

As shown in Figure 1, numerical calculations were performed for stationary GTA welding of stainless steel with

Table I. Thermophysical Properties of 304 Stainless Steel[14,19,28] and Welding Conditions

Nomenclature	Symbol	Value (Unit)
Constant, in Eq. [15]	A_v	2.52
Specific heat of solid phase	c_s	700 (J kg^{-1} K^{-1})
Specific heat of liquid phase	c_l	780 (J kg^{-1} K^{-1})
Mass diffusion coefficient of solid phase	D_s	$\cong$0
Mass diffusion coefficient of liquid phase	D_l	3×10^{-5} (cm^2 s^{-1})
Thermal conductivity of solid phase	k_s	22 (W m^{-1} K^{-1})
Thermal conductivity of liquid phase	k_l	22 (W m^{-1} K^{-1})
Density of solid phase	ρ_s	7200 (kg m^{-3})
Density of liquid phase	ρ_l	6900 (kg m^{-3})
Thermal expansion coefficient	β_T	4.95×10^{-5} (K^{-1})
Solutal expansion coefficient	β_s	0.2
Radiation emissivity	ε	0.4
Dynamic viscosity	μ_l	0.006 (kg m^{-1} s^{-1})
Latent heat of fusion	H	2.47×10^5 (J kg^{-1})
Magnetic permeability	μ_0	1.26×10^{-6} (H m^{-1})
Solidus temperature	T_s	1670 (K)
Liquidus temperature	T_l	1723 (K)
Ambient temperature	T_∞	293 (K)
Reference temperature	T_0	2400 (K)
Reference sulfure concentration	f_l^∞,0	55 (ppm)
Convective heat-transfer coefficient	h_c	80 (W m^{-2} K^{-1})
Latent heat of vaporization	H_v	73.43×10^5 (J kg^{-1})
Gas constant	R	8314.3 (J kg^{-1} mole^{-1})
Stefan–Boltzmann constant	σ	5.67×10^{-8}(W m^{-2} K^{-4})
Electrical conductivity	σ_e	7.14×10^5 (Ω^{-1} m^{-1})
Arc heat flux distribution parameter	σ_q	3.75×10^{-3} (m)
Arc efficiency	η	0.85
Welding voltage	u_w	12 (V)
Welding current	I	150 (A)

dimensions of $L = 15$ mm and $Z = 5$ mm. The thermophysical properties of type 304 stainless steel and welding conditions used in the present study are summarized in Table I. Calculations of heat transfer and fluid flow in the metal begin when the arc is turned on ($t = 0$) and continue until the arc is turned off, at a time of 5 seconds. In one case, calculations are continued after the arc is turned off to find the nature of heat transfer and fluid flow during the solidification process.

A. *When the Sulfur Concentration is Zero*

Figure 3 shows the velocity vectors and streamline contours under the extreme case when the sulfur concentration is zero ($S = 0$ ppm) at times of 2 through 5 seconds. Two curves representing, respectively, the liquidus line (at 1727 K) and solidus line (at 1670 K)[28] are also shown in the velocity-vector plot after 5 seconds. The small size of the

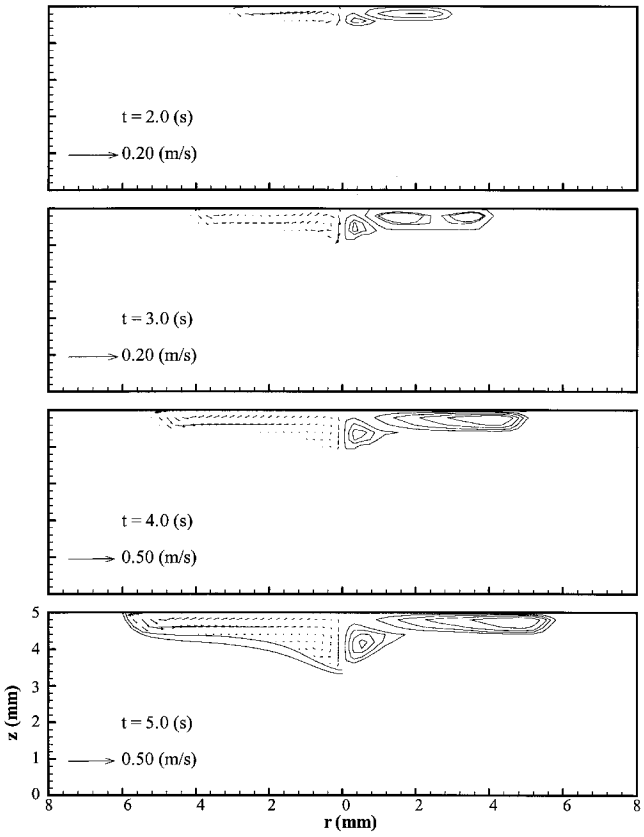

Fig. 3—Velocity vectors and streamline contours at different times; S = 0 ppm.

mushy zone confirms our former assumptions that the solid-phase velocity and the interdendritic flow of solute–rich/poor liquid in the mushy zone are negligible. It is seen that, generally, there are two vortexes: one is clockwise and near the center, caused by the electromagnetic force; and the other is counterclockwise and nearly parallel to the top free surface, caused by the negative surface-tension temperature gradient ($\partial\gamma/\partial T < 0$). Due to the assumed Gaussian distribution of the incident thermal flux, the maximum surface temperature occurs at the center of the weld pool, as seen in Figure 4. Hence, the surface tension increases outward from the center as the temperature decreases outward, causing the liquid metal at the surface to flow outward and creating the counterclockwise vortex. The outward flow at the surface can be better seen from the corresponding top-viewed flow patterns and isotherms, shown in Figure 5 at a time of 5 seconds. Because the heat from the arc is carried by the outward flow, the width of the weld pool increases significantly with time. On the other hand, the clockwise vortex carries heat from the top surface downward, creating pool penetration, although it is small under the present conditions. Hence, when the 304 stainless steel contains no sulfur, the weld pool exhibits shallow penetration and a large width-to-depth ratio.

B. *Effect of Sulfur Concentration*

The velocity vectors and streamline contours are shown in Figure 6 for metals containing 100 ppm of sulfur (S = 100 ppm). It is noted that the temperature with the maximum

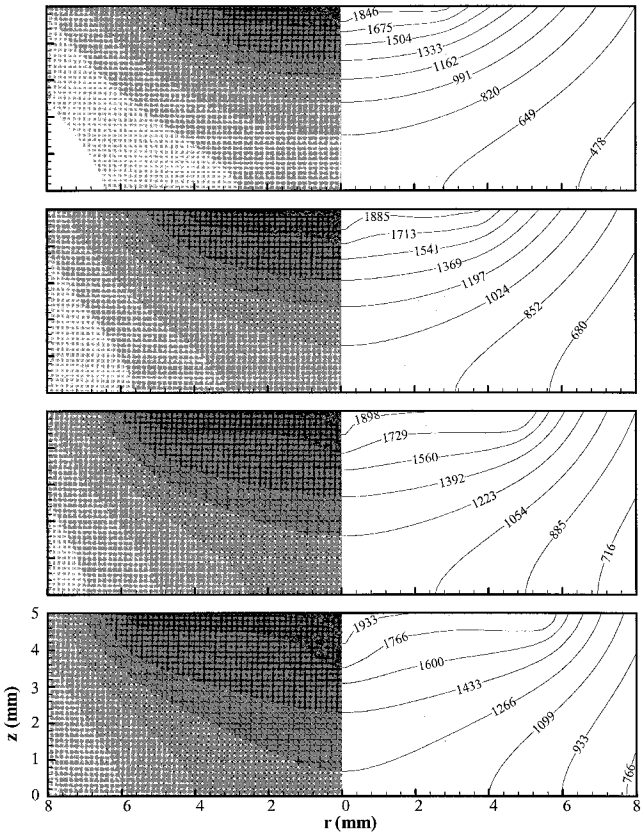

Fig. 4—Temperature shading and isotherms (K) at different times; S = 0 ppm.

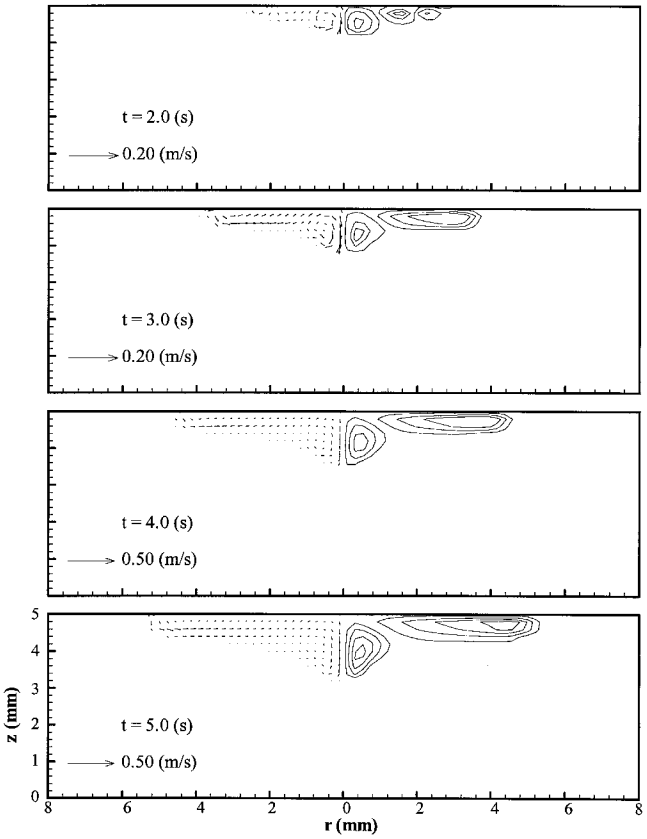

Fig. 6—Velocity vectors and streamline contours at different times; S = 100 ppm.

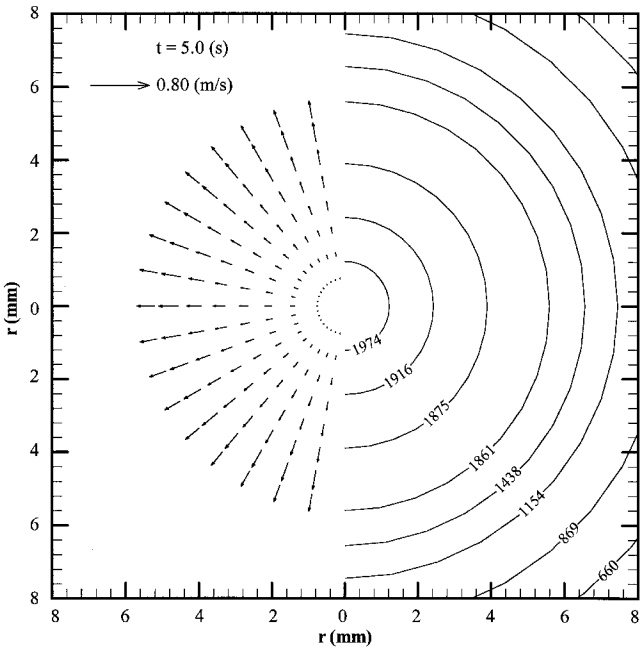

Fig. 5—Top view of velocity vectors and isotherms (K) at t = 5 s; S = 0 ppm.

surface tension is about 1968 K for a 100 ppm sulfur concentration, as seen in Figure 2. When the metal is heated, melted, and between the temperatures of 1727 and 1968 K, the maximum surface tension occurs at the center of the pool (because the center temperature is the highest), as shown in Figure 7. As a result, during this period of time, there is a surface-tension force pulling the fluid toward the center and then downward. Basically, the flow patterns in Figure 6 are similar to those shown in Figure 3, except that at a time of 2 seconds, the flow in Figure 6 appears to be a little random, and the penetration depth is greater for the case with S = 100 ppm. The top views of the velocity vectors and isotherms at times of 2 and 5 seconds are plotted in Figures 8(a) and (b), respectively. It is seen that, at t = 2 s (Figure 8(a)), the maximum surface tension occurs neither at the center of the weld pool nor at the edge.

However, as the time increases, the surface temperature increases so that the maximum surface tension shifts to near the edge of the weld pool, leading to an outward flow at a time of 5 seconds (Figure 8(b)). From Figure 2, with the increase of sulfur concentration, the maximum surface tension shifts from the left (lower temperatures) to the right (higher temperatures). Hence, to reach the maximum surface tension, it requires a longer welding time for metals containing a higher amount of sulfur. Also during this period of time, the maximum temperature (and the surface tension) occurs at the center of the weld pool, creating an inward flow. This explains why the penetration depth in Figure 6 for S = 100 ppm is greater than that in Figure 3 for S = 0 ppm. However, when the weld-pool surface temperature exceeds the temperature corresponding to the maximum surface tension, the point with the maximum surface tension starts to move from the center to the edge of the weld pool. As the point with the maximum surface tension moves

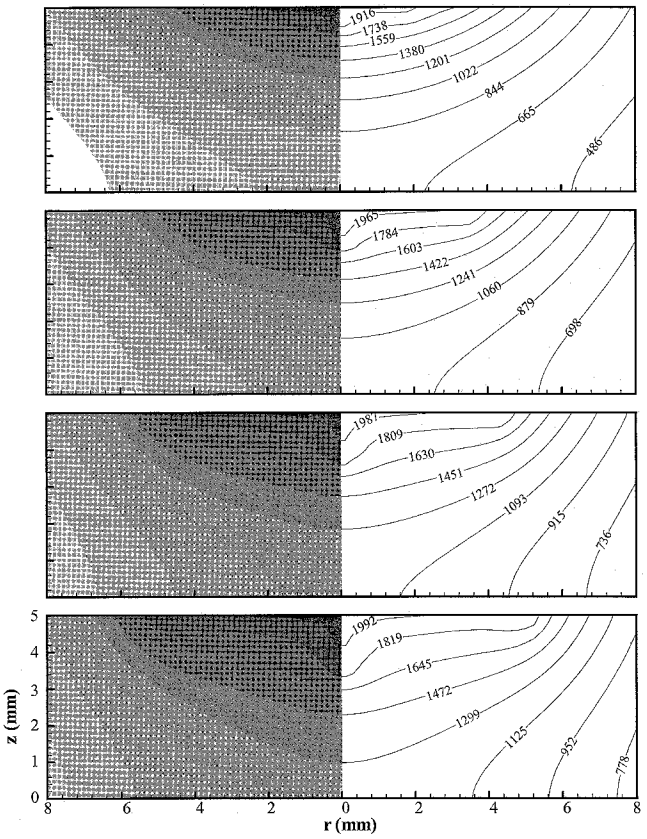

Fig. 7—Temperature shading and isotherms (K) at different times; S = 100 ppm.

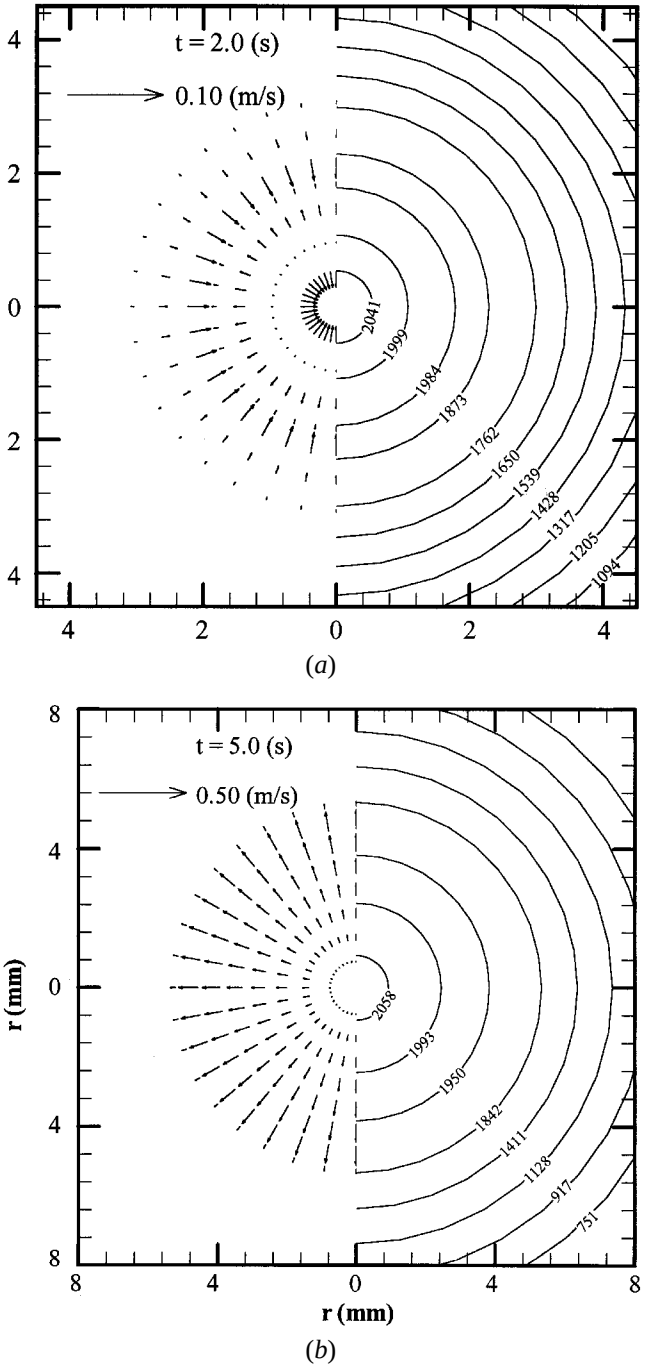

Fig. 8—Top view of velocity vectors and isotherms (K) at (*a*) *t* = 2 s and (*b*) *t* = 5 s; S = 100 ppm.

between the center and the edge of the weld pool, more-complicated flow patterns can be expected.

Figure 9 shows a sequence of flow patterns and streamline contours when the metal contains 155 ppm sulfur (S = 155 ppm). The corresponding temperature distributions are given in Figure 10. It is noted that the maximum surface tension occurs at about 2039 K (Figure 2) for S = 155 ppm. The surface locations at which fluid flow from both sides meet (which is usually the location with the maximum surface tension) at times of 2 through 5 seconds are indicated, respectively, by the letters A through D in the figure. It is noted that the point with the maximum surface tension moves outward with time. At a time of 2 seconds, as the maximum surface temperature is still below 2039 K (Figure 10), the maximum surface tension is located at the center (point A), creating an inward flow at the surface. This can clearly be seen in the corresponding top view of the flow pattern (Figure 11(a)).

At a time of 3 seconds, the location with the maximum surface tension moves to point B, between the center and the edge of the weld pool. Hence, an inward flow from the edge to point B and an outward flow from the center to point B are created (Figure 11(b)), although the outward flow is smaller than the inward flow. As a result, a clockwise vortex is created near the edge at the left-hand side of point B, while a counterclockwise vortex is created at the right-hand side of point B. However, the counterclockwise vortex is squeezed upward by a stronger clockwise vortex near the center, created by the electromagnetic force. The flow patterns at the surface of the weld pool at the times of 4 and 5 seconds are given, respectively, in Figures 11(c) and (d). The squeezed counterclockwise vortex becomes more visible at a time of 5 seconds. Hence, the complicated flow phenomenon consisting of three vortexes is created in the weld pool when the metal contains 155 ppm sulfur. As the heat flux from the arc is "dispersed" by the three vortexes, the penetration depth is limited.

With a little increase in sulfur, from S = 155 to 160 ppm, a nearly full–penetration weld pool is created at a time of 5 seconds, as shown in Figure 12. It is noted that, for S = 160 ppm, the temperature with the maximum surface tension is about 2044 K. After 5 seconds of heating, the surface

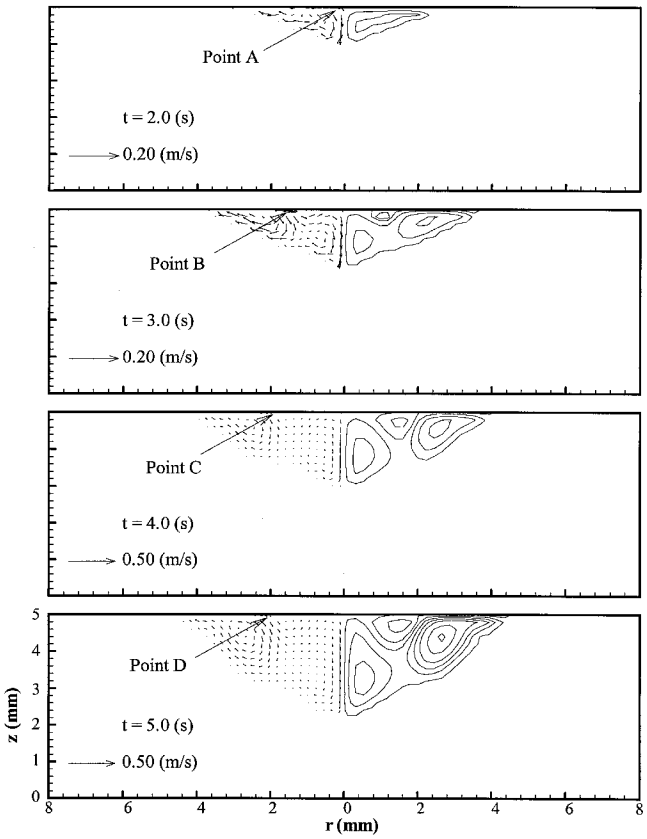

Fig. 9—Velocity vectors and streamline contours at different times; S = 155 ppm.

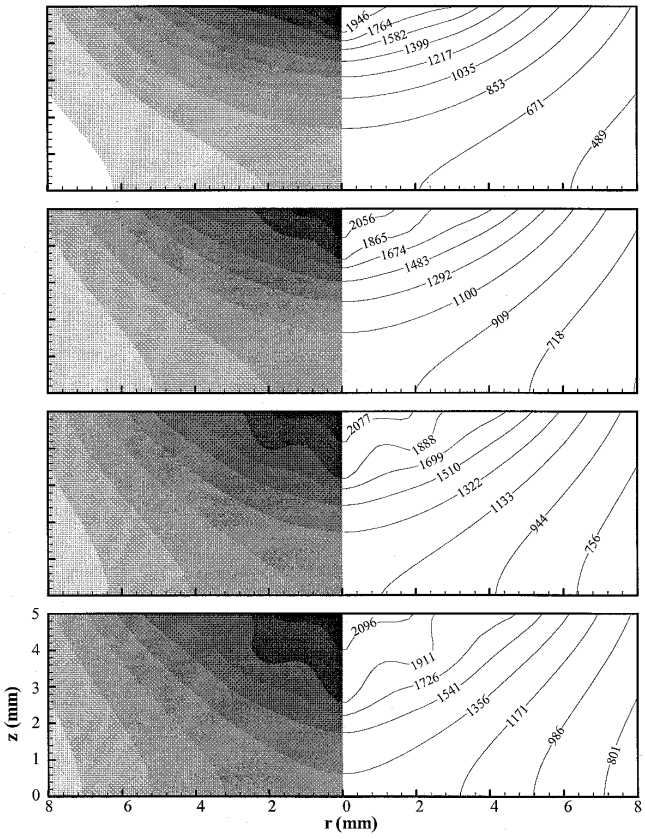

Fig. 10—Temperature shading and isotherms (K) at different times; S = 155 ppm.

temperatures are still below 2044 K (Figure 13), so that the maximum surface tension occurs at the center of the weld pool, creating an inward flow (Figure 14). Hence, there is only one large clockwise vortex carrying the heat from the arc and creating a deep penetration. In fact, the large vortex can be considered as a combination of two clockwise vortexes: one resulting from the surface tension and the other from the electromagnetic force. By comparing Figures 7, 10, and 13, it is interesting to see that the maximum surface temperature occurs when S = 155 ppm. This is because when S = 100 ppm, the heat flux from the arc is carried outward to increase the width of the weld pool, while at S = 160 ppm, the flux is carried downward to increase the depth. Neither phenomenon occurs when S = 155 ppm. With a small increase in sulfur concentration, from 155 to 160 ppm, an abrupt change in the flow pattern and full penetration is achieved. The 160 ppm sulfur concentration can be considered as the threshold concentration for the welding conditions used in the present study. It is noted that the surface-temperature distribution and its maximum value depend upon the welding conditions, such as the welding current, arc energy distribution, *etc.* Hence, the threshold sulfur concentration depends upon the welding conditions. It is reasonable to expect that a higher sulfur concentration facilitates deeper penetration. However, only a very small increase in penetration is found (Figure 15) when the sulfur concentration is increased to S = 300 ppm. As higher sulfur concentrations are expected to increase the susceptibility to solidification hot cracking, a minimum sulfur concentration is desirable as long as full penetration can be achieved.

The results discussed previously can be summarized by the following three cases.

1. *Case 1: Steels with a zero or low sulfur content*

In this case, the maximum surface tension occurs near the edge of the weld pool, and there are two vortexes. One vortex, clockwise, near the center of the weld pool, is created by the electromagnetic force; the other vortex, counterclockwise, very narrow, and near the surface of the weld pool, is created by a negative surface-tension temperature gradient. The thermal energy from the arc is carried outward, resulting in a wide but shallow weld pool with a higher width-to-depth ratio.

2. *Case 2: Steels with a medium sulfur content (about 150 ppm)*

In this case, the maximum surface tension occurs at a location between the center and the edge of the weld pool, and there are three vortexes. The first one, clockwise, near the center of the weld pool, is created by the electromagnetic force. The second, clockwise, near the edge of the weld pool, is created by the positive surface-tension gradient, *i.e.*, $\partial\gamma/\partial T > 0$. The third one, counterclockwise, located in between the aforementioned two vortexes, is created by a negative surface-tension gradient. As the thermal energy from the arc is not efficiently carried downward or outward due to the complicated flow patterns, the weld penetration depth and width are medium.

3. *Case 3: Steels with a high sulfur content (about 300 ppm)*

In this case, the maximum surface tension occurs at the center of the weld pool and with only one vortex. This large,

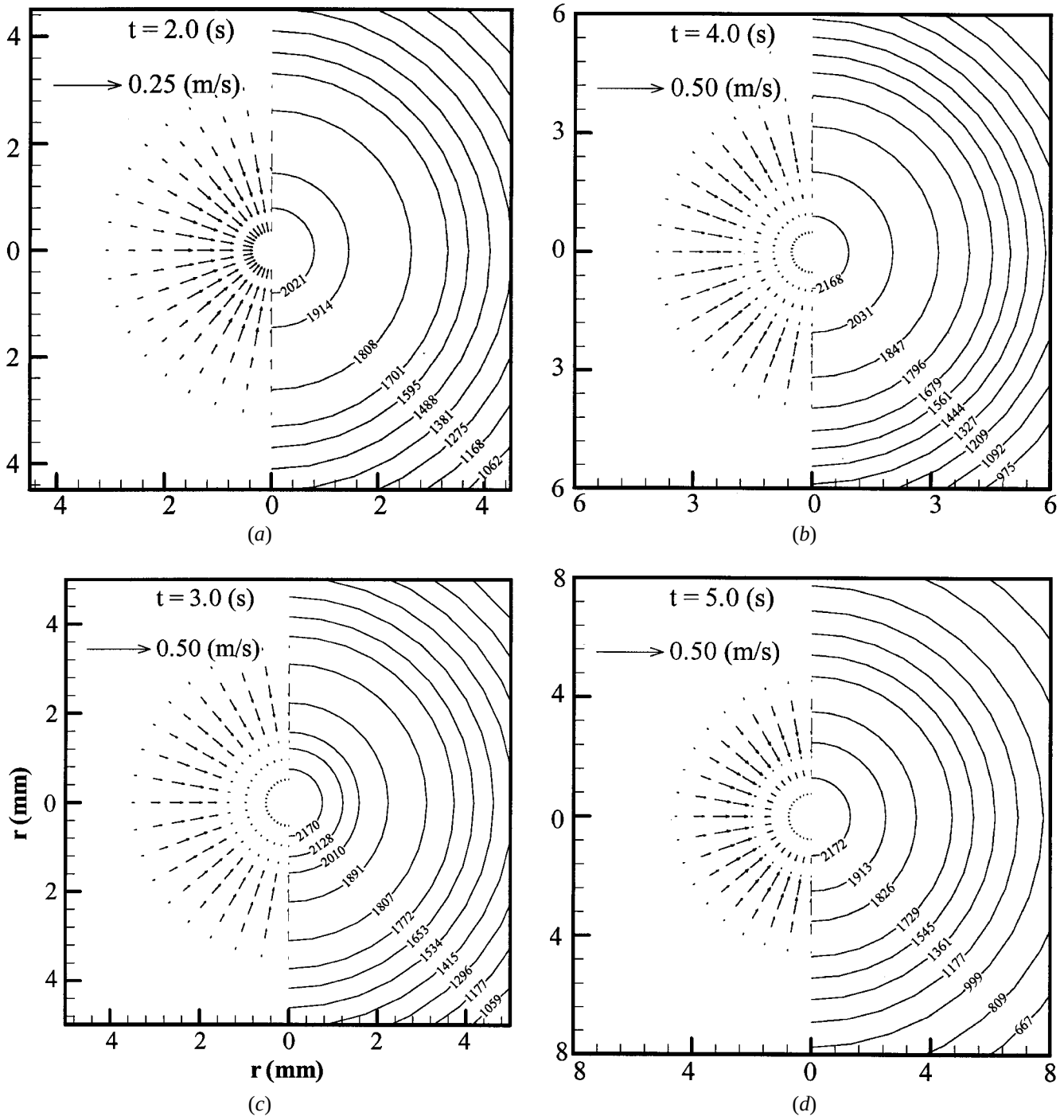

Fig. 11—Top view of velocity vectors and isotherms (K) at (*a*) $t = 2$ s, (*b*) $t = 3$ s, (*c*) $t = 4$ s, and (*d*) $t = 5$ s; S = 155 ppm.

clockwise vortex is a combination of two vortexes caused, separately, by the electromagnetic force and the positive surface-tension temperature gradient. The thermal energy from the arc is efficiently carried downward by the flow, creating a deeper weld pool.

To find how fast the weld pool solidifies, when the arc is turned off at a time of 5 seconds (as in Figure 12 for S = 160 ppm), the flow patterns and isotherms during solidification are given in Figure 16 at times of 5.1 and 5.2 seconds. Due to heat losses to the surroundings at the top surface, there is a "hot spot" within the solidified weld bead. If a hot spot (*i.e.*, the location where the metal is last solidified) occurs at the interior of the weld pool, shrinkage defects can possibly occur. It is noted that it takes only about 0.3 seconds to obtain a complete solidification after the arc is turned off. This is consistent with the assumption made before, *i.e.*, there is no time to create the interdendritic fluid flow for the formation of macrosegregation in the weld pool.

C. *Effect of Electromagnetic Force*

The effects of electromagnetic force on fluid flow and weld penetration can be studied by nullifying the last term in both Eqs. [2] and [3]. Figure 17 shows a sequence of

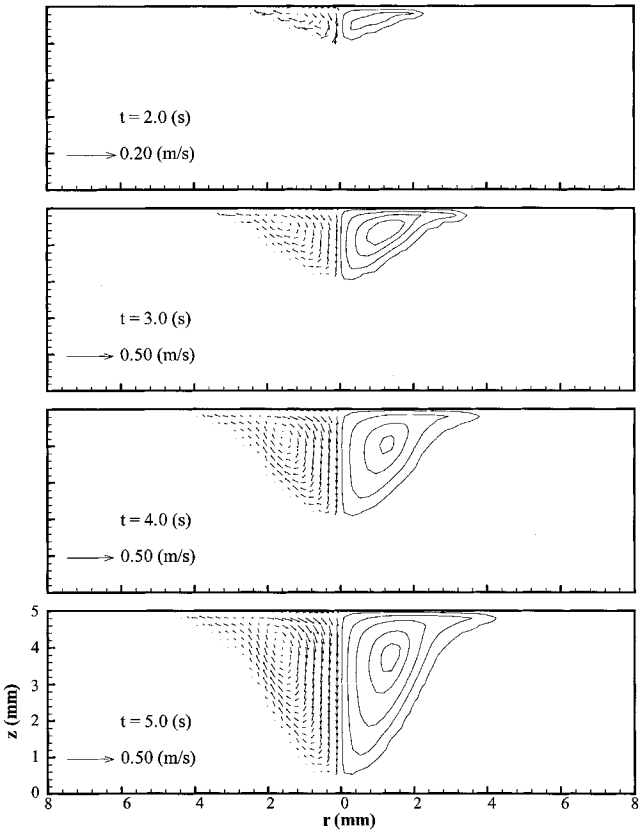

Fig. 12—Velocity vectors and streamline contours at different times; S = 160 ppm.

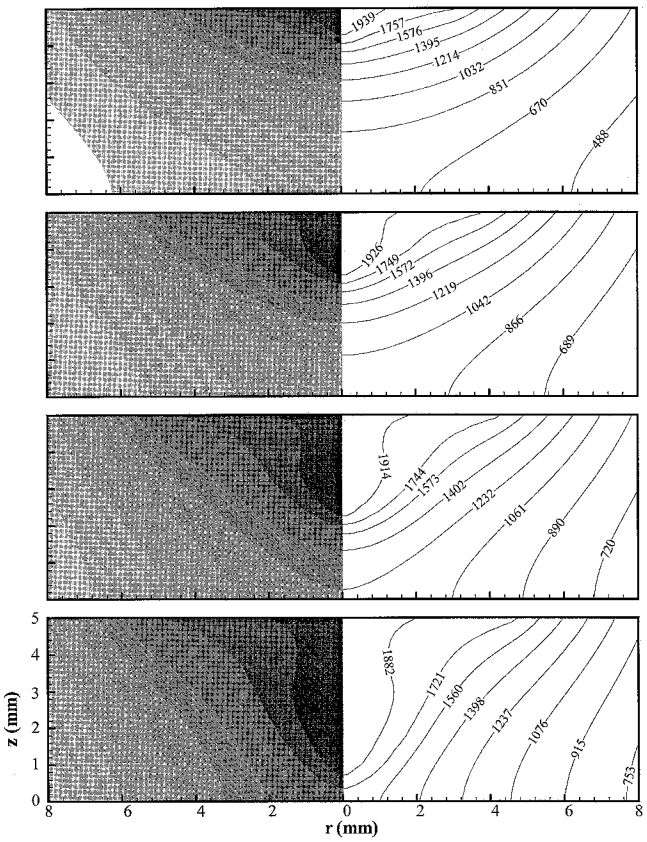

Fig. 13—Temperature shading and isotherms (K) at different times; S = 160 ppm.

fluid-flow patterns and streamline contours at different times, when S = 160 ppm. The corresponding isotherms are plotted in Figure 18. As mentioned previously, the electromagnetic force creates a clockwise vortex at the center of the weld pool. Without the electromagnetic force, there is nearly no flow at the center of the weld pool until, at $t = 5$ s, a large clockwise vortex near the center of the weld pool is suddenly created. This vortex is caused solely by the surface tension. Figure 19 shows the very small flow velocities at the top surface near the center of the weld pool at times of 3 and 4 seconds. By comparing Figures 17 and 12, it is interesting to note that, although significant differences exist before $t = 4$ s, the final flow patterns and penetration depths at $t = 5$ s are similar for the cases with or without the electromagnetic force. The smaller penetration depth in Figure 17 is due to the assumption that the electromagnetic force is neglected.

D. *Effect of Surface Tension*

To study the effects of surface tension on fluid flow and weld penetration, the surface-tension boundary condition (*i.e.*, the first expression of Eq. [10]) is set to zero. Calculations were performed for the case in which the sulfur concentration is 160 ppm. In fact, as the effect of sulfur concentration is ignored, the calculated results are valid for any sulfur concentration. Figure 20 shows a clockwise vortex near the center of the weld pool. Although the penetration depth is comparable, the flow velocities are much smaller than those in Figure 12. As seen in the corresponding isotherms (Figure 21), the temperatures are much higher than those in Figure 13. In fact, the metal was "burned through" by the high temperature, and the heat from the arc was transferred downward, partially by heat conduction. The maximum surface velocity occurs at the center of the weld pool, as seen in the top-view plot (Figure 22). This is understandable, because the flow is caused only by the electromagnetic force. By comparing Figures 12, 17, and 20, it is found that at $t = 5$ s, the fluid flow is influenced more by the surface tension, while the surface tension and the electromagnetic force equally contribute to weld penetration.

E. *Effect of Welding Current*

Calculations were performed for several welding currents to study the effect of the welding current on flow patterns and weld penetration when the metal contained 160 ppm sulfur. Two typical results are presented here; one is for $I = 125$ A (Figure 23) and the other is for $I = 175$ A (Figure 24). In Figure 23, although a single clockwise vortex is formed, the weld penetration is limited because less heat is available from a smaller-current arc. This can also be seen from the isotherm plots, which show that the temperatures in the weld pool are relatively low compared to those in Figure 13. The result implies that although surface tension is important for deep penetration, a minimum current is needed in order to provide the required heat source. When the welding current is increased to 175 A, it is surprising to see that the weld penetration decreases (Figure 24, as

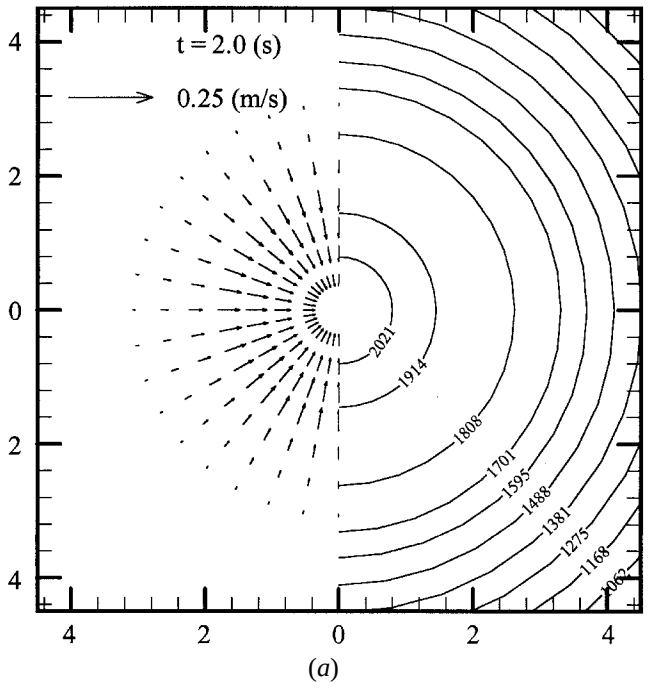

(*a*)

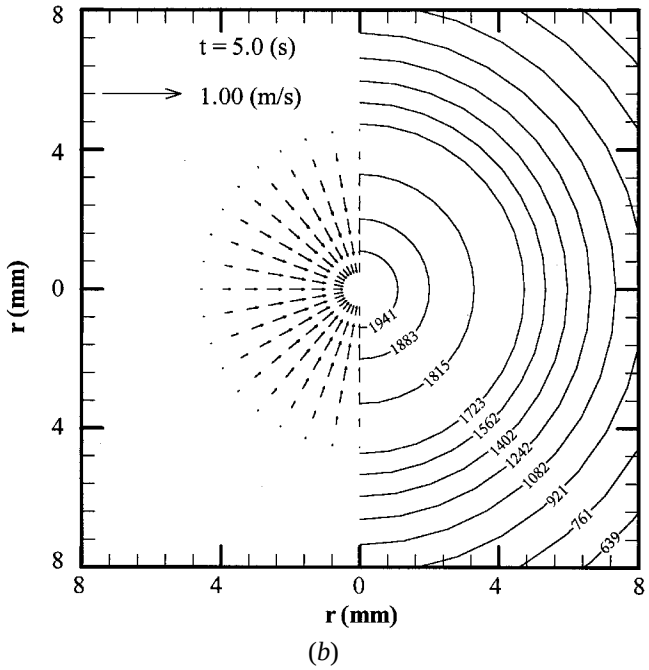

(*b*)

Fig. 14—Top view of velocity vectors and isotherms (K) at (*a*) t = 2 s and (*b*) t = 5 s; S = 160 ppm.

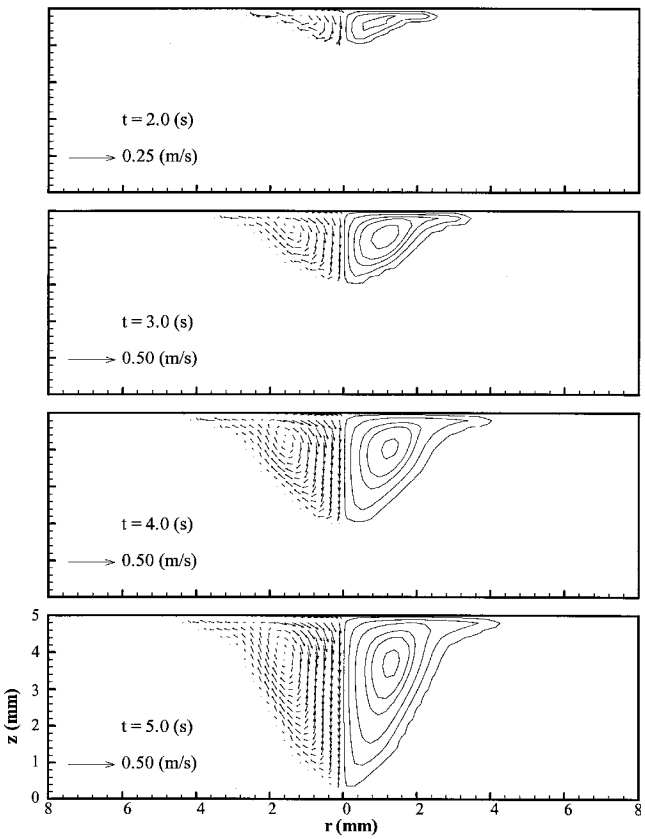

Fig. 15—Velocity vectors and streamline contours at different times; S = 300 ppm.

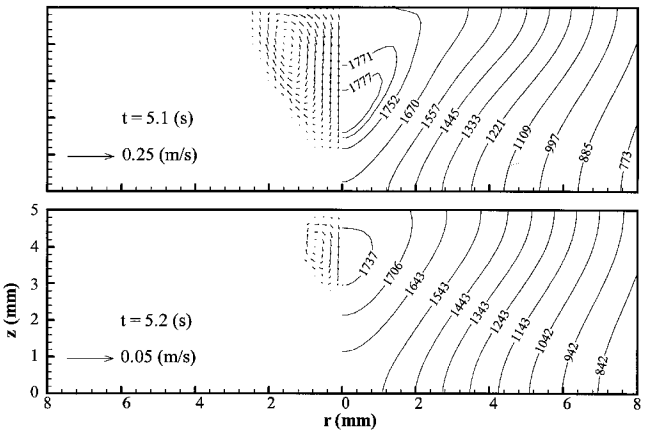

Fig. 16—Velocity vectors and isotherms (K) during solidification after the arc is turned off at t = 5 s; S = 160 ppm.

compared to Figure 12) when the welding current is 150 A. The result shows that by increasing the welding current, there is no guarantee that the penetration depth will also be increased. However, this phenomenon can well be explained by the use of Figure 2. At I = 175 A, the temperatures near the center of the weld pool (note the isotherm plots in Figure 24) exceed the temperature of the maximum surface tension (2044 K). Hence, the point with the maximum surface tension is near the edge of the weld pool (instead of near the center of the weld pool, as in Figures 12 and 13), leading to an outward flow, similar to the case with S = 100 ppm. As a result, the weld pool is wider but shallow, as compared to Figure 12. The previous discussion further illustrates that the threshold sulfur concentration depends on the combined effect of several welding parameters, as previously discussed.

F. *When Two Metals with Different Sulfur Concentrations Are Welded Together*

In this case, the welding conditions are no longer axisymmetrical; the governing equations and the associated boundary conditions (for example, Eqs. [2], [3], and [9]) should be

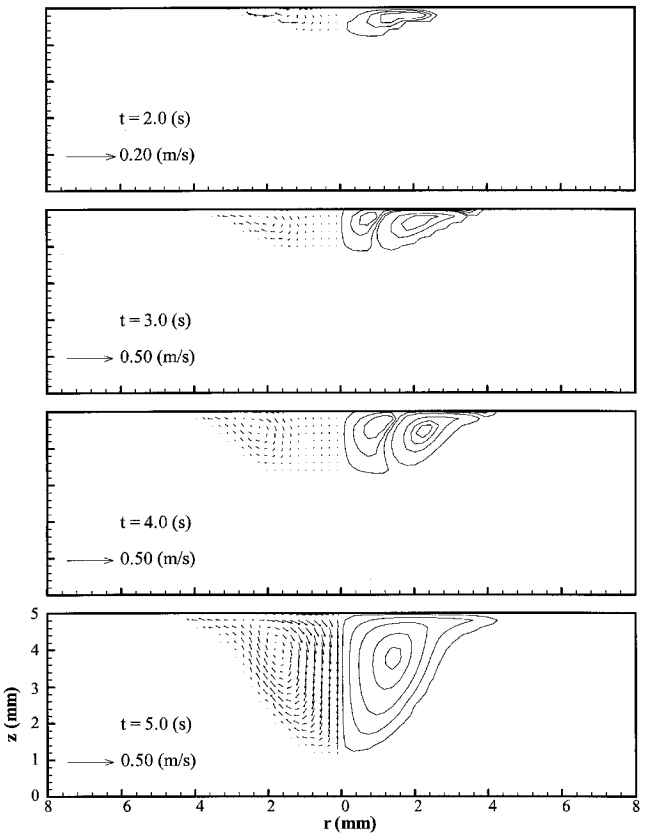

Fig. 17—Velocity vectors and streamline contours at different times if the electromagnetic force is neglected; S = 160 ppm.

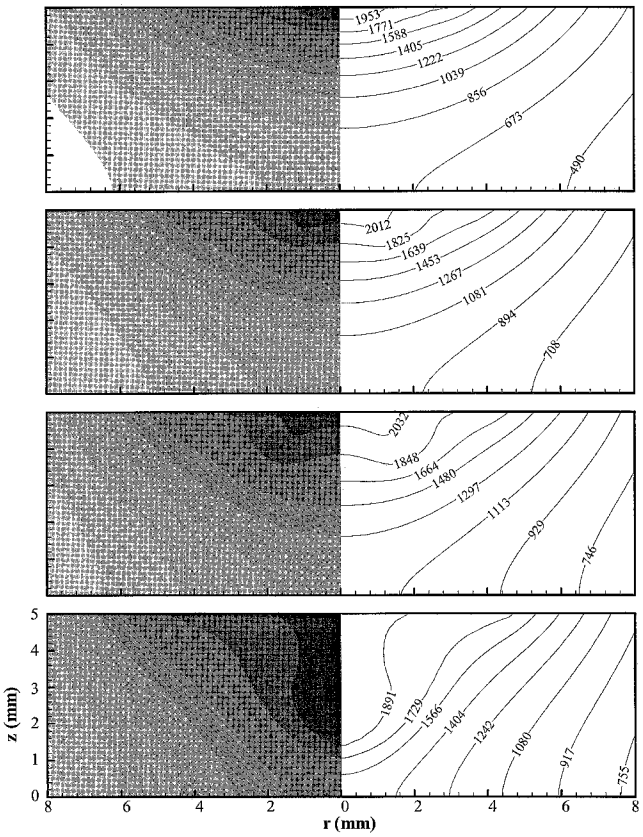

Fig. 18—Temperature shading and isotherms (K) at different times if the electromagnetic force is neglected; S = 160 ppm.

modified to become two-dimensional in the $x - y$ Cartesian coordinate system. In addition, the sulfur distribution in the weld pool can be calculated *via*
Species

$$\frac{\partial}{\partial t}(\rho f^{\alpha}) + \nabla \cdot (\rho \mathbf{V} f^{\alpha}) = \nabla \cdot (\rho D \nabla f^{\alpha}) + \nabla \cdot (\rho D \nabla (f_l^{\alpha} - f^{\alpha})) - \nabla \cdot (\rho (\mathbf{V} - \mathbf{V}_s)(f_l^{\alpha} - f^{\alpha})) \quad [34]$$

where the mass fraction of the sulfur and the mass diffusivity are defined as

$$f^{\alpha} = f_s f_s^{\alpha} + f_l f_l^{\alpha};\ D = f_s D_s + f_l D_l \quad [35]$$

Again, the physical meanings of each term in Eq. [34] are given by Diao and Tsai,[25] and they will not be repeated here. Numerical calculations were performed for two plates welded together at $x = 0$; one with a 50 ppm sulfur concentration (on the left-hand side) and the other with 200 ppm (on the right-hand side).

Figure 25 shows the flow patterns at different times, and the corresponding isotherms are plotted in Figure 26. It is seen that two vortexes are created; the one on the right-hand side is larger, while a smaller vortex exists on the left-hand side. The entire weld pool is skewed toward the left, where there is a lower sulfur concentration. The phenomenon can be well explained with the help of Figure 2. The maximum surface temperature, which is about 1950 K, is located initially at the center where the two metals are joined (Figure 26). For the metal containing 50 ppm sulfur, the maximum surface tension (at 1862 K) is not located at the center; instead, it is located at a point, (for example, point A) between the left edge of the weld pool and the center. In other words, at point A, there is a net force pulling fluid from both its left- and right-hand sides. For the metal containing 200 ppm sulfur at a temperature of 1950 K, the point with the maximum surface tension is located at the center, creating a flow to the left-hand side. It is noted, for metals containing 200 ppm sulfur, that the temperature with the maximum surface tension is 2082 K (Figure 2).

In addition, as the surface tension in metals containing 50 ppm sulfur is greater than that for metals containing 200 ppm sulfur, point A has the maximum surface tension for the entire top surface. The net result is a force pulling fluid toward point A from both its sides and then downward, creating a larger vortex at its right-hand side and a smaller vortex at its left-hand side. Apparently, the surface tension is so strong that the electromagnetic force acting downward at the center of the weld pool is "twisted." The entire weld pool is skewed to the left-hand side, resulting in a shallow penetration on the right-hand-side metal and a little deeper penetration on the left-hand-side metal. It is noted that potential welding failure can occur if the fusion zone in the right-hand-side metal is too small. The phenomenon of a skewed weld pool was discovered experimentally when two metals containing different sulfur concentrations were welded together.[23,24]

In Figure 26, it is seen that the highest-temperature "hot spot" is skewed toward the left-hand side for the metal with

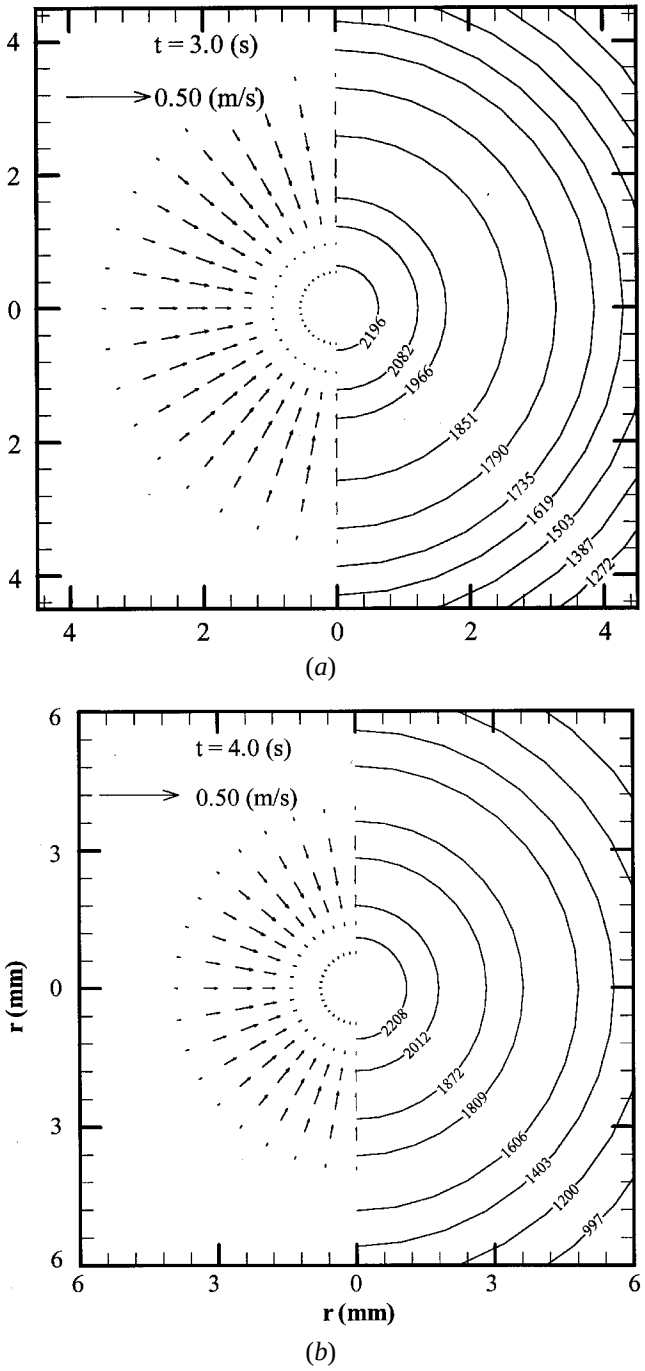

Fig. 19—Top view of velocity vectors and isotherms (K) at (*a*) $t = 3$ s and (*b*) $t = 4$ s if the electromagnetic force is neglected; S = 160 ppm.

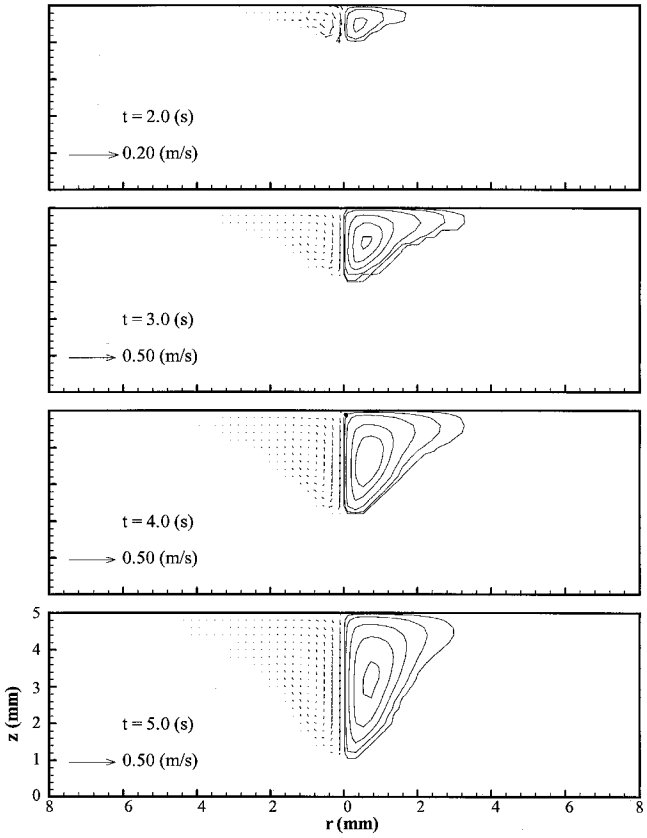

Fig. 20—Velocity vectors and streamline contours at different times if the surface tension is neglected; S = 160 ppm.

the smaller sulfur concentration. This, of course, is caused by the fact that the thermal energy from the arc at the top surface is carried to the left-hand side by the flow patterns, as shown in Figure 25. Figure 27 shows the final sulfur distribution when the weld pool is completely solidified. It is clearly seen that part of the sulfur in the right-hand side sulfur-rich metal is carried by the flow to the left-hand-side metal. The macroscopic "mixing effect" is caused by the fluid flow produced by the interaction between the surface tension and the electromagnetic force.

G. *General Discussion on the Predicted Results*

There is no doubt that it is rather difficult to conduct experiments in the welding process for the purpose of validating theoretical predictions. Real-time measurements of fluid-flow velocity in the weld pool are especially difficult, if not impossible. This is because not only does a welding process involve high temperatures, nontransparent metals, short durations, smoke, and small weld beads, but, also, the presence of the welding arc may interfere with measuring instruments. Hence, few experimental data under rather limited conditions are available. These include the determination of the shape and penetration of the solidified weld pool[7,12] and the real-time measurements of the weld-pool surface temperature.[33,34] Unfortunately, the published experimental data do not provide sufficient information for the purpose of accurate and meaningful "validation" of the theoretical predictions, especially fluid-flow patterns. Nevertheless, the flow patterns predicted by the present study are generally consistent with those proposed based on the experimental studies.[3,22,23] Furthermore, the important features of our predictions, such as the existence of two vortexes, are also similar to the theoretical predictions by Zacharia *et al.*[12] and Choo and Szekely.[18]

Generally speaking, four major factors could affect the modeling predictions of the present study. They are (1) the mathematical model, (2) the numerical method, (3) the thermophysical properties and welding parameters, and (4) the reliability of the surface tension–temperature–sulfur content

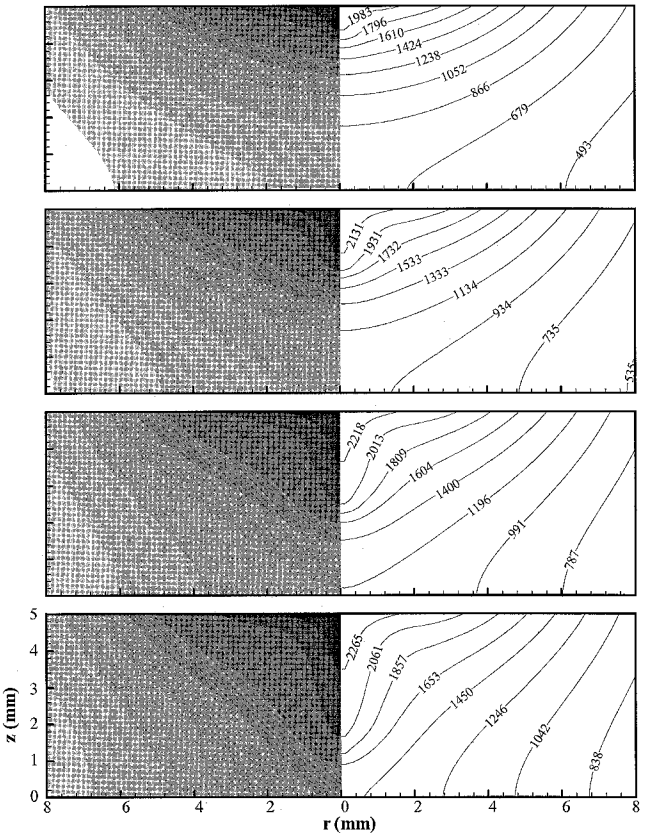

Fig. 21—Temperature shading and isotherms (K) at different times if the surface tension is neglected; S = 160 ppm.

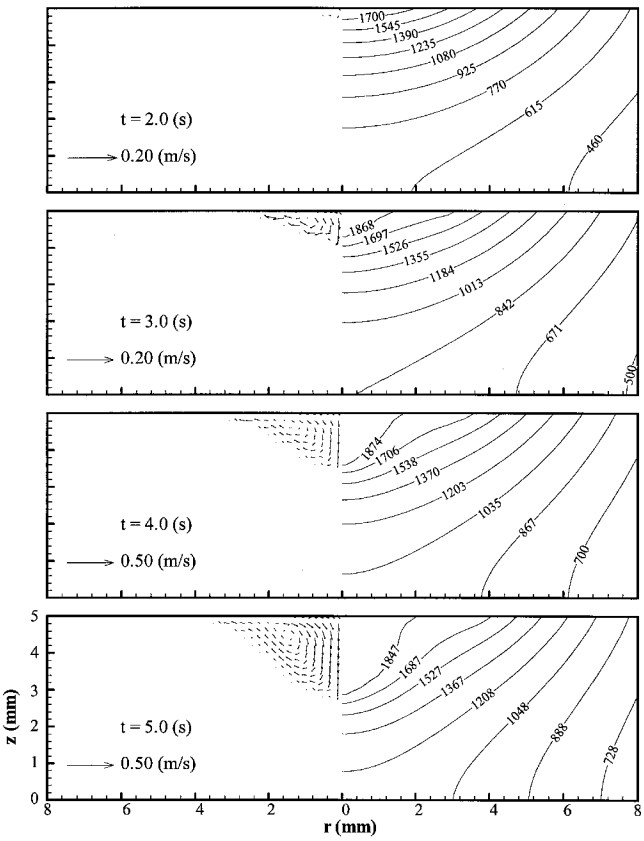

Fig. 23—Velocity vectors and isotherms (K) at different times when the welding current is 125 A; S = 160 ppm.

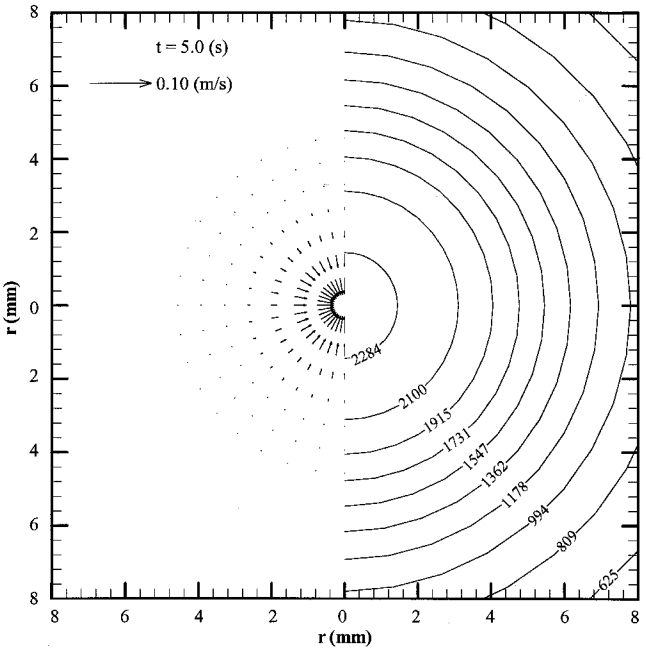

Fig. 22—Top view of velocity vectors and isotherms (K) at t = 5 s if the surface tension is neglected; S = 160 ppm.

relationship. The continuum formulation, used in the present study to handle the heat transfer and fluid flow during melting and solidification, has been widely used and validated.[35]

Although several assumptions have been made in the mathematical model, such as the flat pool surface and the independence of the welding arc on metal flow, it is believed that the mathematical model used in the present study is sound and adequate. In regard to the numerical method, a well established control volume–based, finite-difference method using the SIMPLEC algorithm was used in the present study.[30] In addition, as discussed in Section II–E, when the grid system was refined, the results were found to be very close to the original ones. Although constant thermophysical properties were assumed in the calculation, the assumption will not cause a fundamental change in predictions (of course, it will affect the accuracy of the predicted results).

As fluid flow in the weld pool is dominated by surface tension, the accuracy of the surface-tension formula in Eq. [33] plays a critical role in the correctness of the theoretical predictions. It is noted that Eq. [33] was obtained through "curve fitting" to experimental data.[29] Although it is difficult to accurately measure surface tension as a function of temperature and sulfur concentration, and there is little difference between the fitted curve and the experimental data, the correctness, or at least the trend, of Eq. [33] should not be in doubt.

In conclusion, it is believed that the predictions presented in the present study are reliable as trends, although their accuracy remains to be validated. For example, the "actual" threshold sulfur concentration for full penetration may be 170 ppm instead of 160 ppm, which is predicted by the present model.

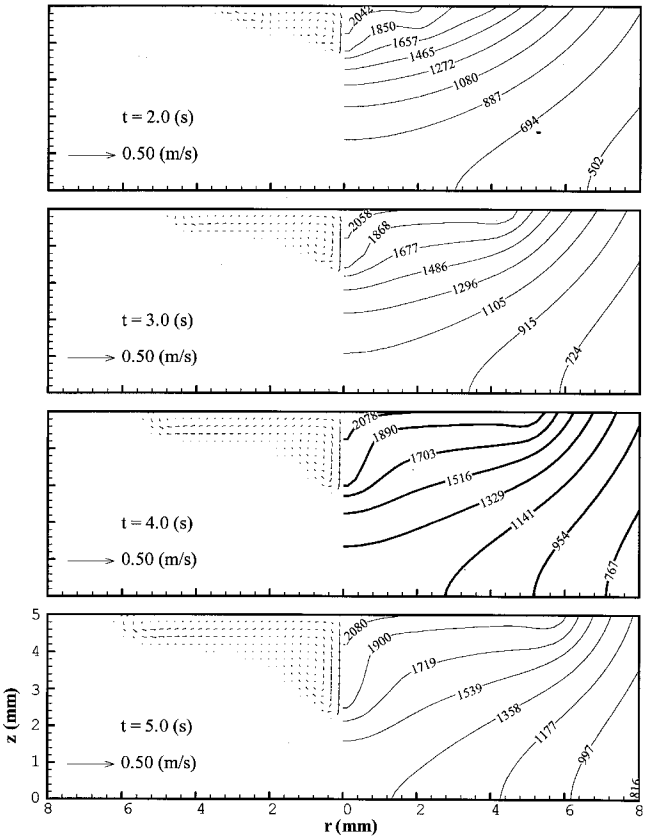

Fig. 24—Velocity vectors and isotherms (K) at different times when the welding current is 175 A; S = 160 ppm.

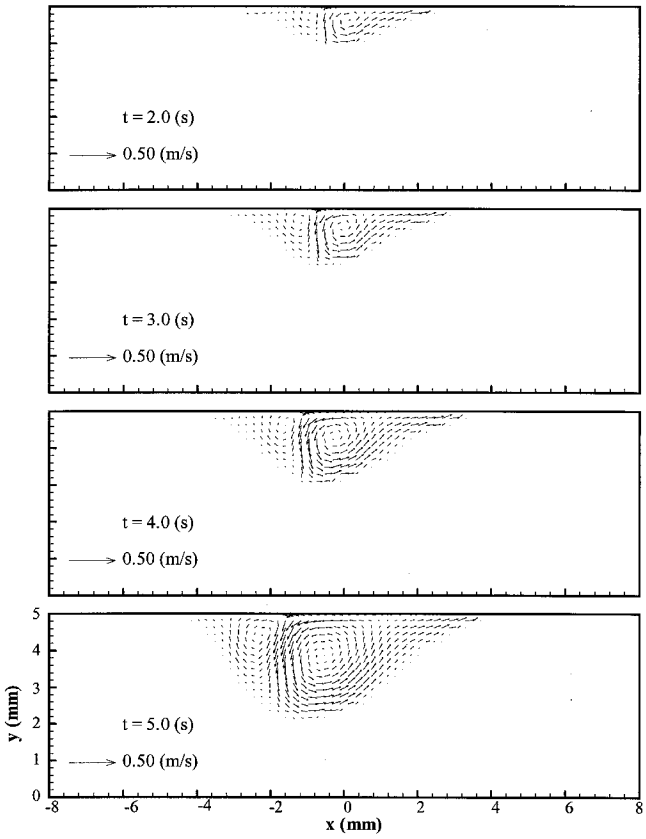

Fig. 25—Velocity vectors at different times when two metals with different sulfur contents are welded together, left-hand-side metal S = 50 ppm, and right-hand-side metal S = 200 ppm.

IV. CONCLUSIONS

The effects of surface tension on metal flow and the resulting weld penetration have been studied theoretically. Although the present study places emphasis on the sulfur concentration in 304 stainless steel, the phenomena predicted should be generally true and applicable to other surface-active elements and alloys as well. For an Fe-S system, under the welding conditions used in present study, the following conclusions can be drawn.

1. Fluid-flow patterns and weld penetration are the result of interactions between the electromagnetic force and the surface tension; the latter is a function of the temperature and sulfur concentration in the melt.
2. Depending upon the sulfur concentration, one, two, and three vortexes, clockwise or counterclockwise, are found in the weld pool. A single large clockwise vortex can efficiently transfer the thermal energy from the arc, creating a deep weld pool.
3. For given welding conditions, there exists a threshold sulfur concentration to achieve full penetration. The threshold sulfur concentration depends upon the welding conditions.
4. The electromagnetic force facilitates a deeper penetration. However, surface tension can have a positive or negative effect on penetration, depending upon the sulfur content of the metal and the welding conditions. A higher current may not increase penetration depth; its effect also depends on the sulfur content of the metal and the welding conditions.
5. When two metals with different sulfur concentrations are welded together, the weld pool is skewed toward the metal with less sulfur content.
6. The aforementioned predicted phenomena are generally consistent with the published experimental and theoretical results.

NOMENCLATURE

A_v	constant, in Eq. [15]
B	magnetic induction vector
B_θ	self-induced azimuthal magnetic field
c	specific heat
C	coefficient, defined in Eq. [8]
c_l	permeability coefficient, defined in Eq. [7]
d	dendrite arm spacing
D	mass-diffusion coefficient
f	mass fraction
g	volume fraction or gravitational acceleration
h	enthalpy
h_c	convective heat-transfer coefficient between the metal and its surroundings
H	latent heat of fusion
H_v	latent heat of vaporization
I	welding current
J	current density vector
J_r	radial current density
J_z	axial current density

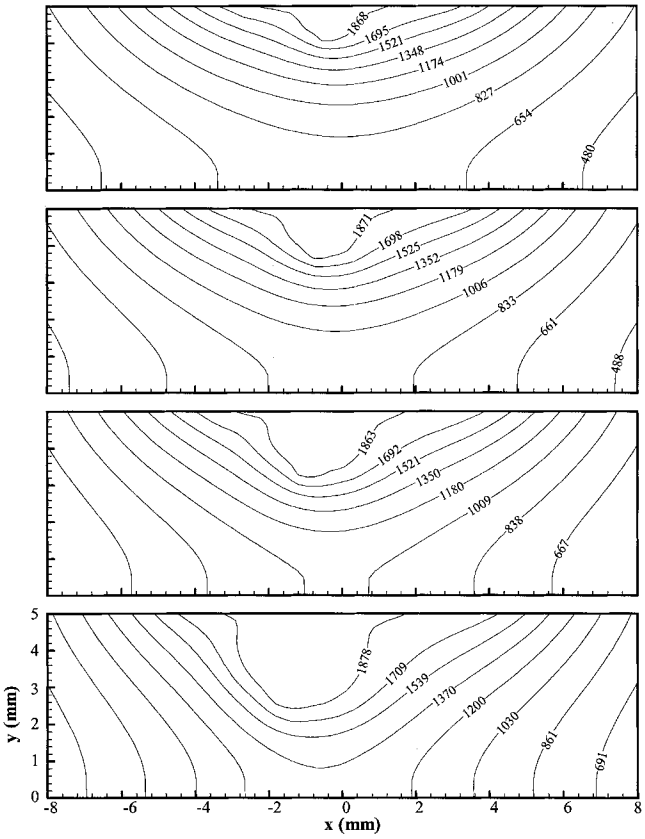

Fig. 26—Isotherms (K) at different times when two metals with different sulfur contents are welded together, left-hand-side metal S = 50 ppm, and right-hand-side metal S = 200 ppm.

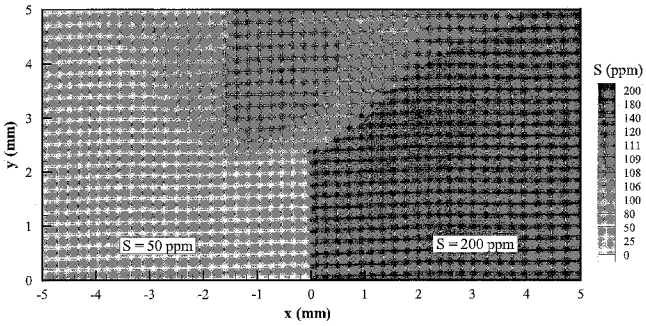

Fig. 27—Final sulfur distribution when the weld pool is completely solidified; left-hand-side metal S = 50 ppm, and right-hand-side metal S = 200 ppm.

k	thermal conductivity
K	permeability, defined in Eq. [7]
p	pressure
P_{atm}	atmospheric pressure
q_{conv}	heat loss by convection
q_{evap}	heat loss by evaporation
q_{radi}	heat loss by radiation
$r - z$	cylindrical coordinate system
R	gas constant
t	time
T	temperature
T_l	liquidus temperature
T_s	solidus temperature
T_∞	ambient temperature
u	velocity in r direction
u_w	arc voltage
v	velocity in z direction
$\mathbf{V}$	velocity vector
$\mathbf{V}_r$	relative velocity vector ($\mathbf{V}_l - \mathbf{V}_s$)
W	melt evaporative rate

Greek symbols

β_s	solutal expansion coefficient
β_T	thermal expansion coefficient
γ	surface tension
$\partial\gamma/\partial f^\alpha$	surface tension concentration gradient
$\partial\gamma/\partial T$	surface tension temperature gradient
ε	surface radiation emissivity
μ_l	dynamic viscosity
μ_0	magnetic permeability
η	arc efficiency
ϕ	electric potential
σ	Stefan–Boltzmann constant
σ_e	electrical conductivity
σ_q	arc heat flux distribution parameter
ρ	density

Subscripts

0	reference value
l	liquid phase
r	relative to solid velocity
s	solid phase

Superscript

α	constituent of alloy

ACKNOWLEDGMENTS

The authors thank Dr. Edward S. Chen, United States Army Research Office (retired), for his encouragement and valuable suggestions during the course of this study. The work was supported by the United States Army Research Office under Grant No. DAAH04-95-1-0136, which is gratefully acknowledged.

REFERENCES

1. G.W. Oyler, R.A. Matuszesk, and C.R. Garr: *Welding J.*, 1967, vol. 46, pp. 1006-11.
2. C.R. Heiple, R.J. Cluley, and R.D. Dixon: in *Physical Metallurgy of Metal Joining*, R. Kossowsky and M.E. Glicksman, eds., TMS-AIME, Warrendale, PA, 1980, pp. 160-65.
3. C.R. Heiple and J.R. Roper: *Welding J.*, 1981, vol. 60, pp. 143s-145s.
4. C.R. Heiple, P. Burgardt, and J.R. Roper: *Modeling of Casting and Welding Process II*, J.A. Dantzig and J.T. Berry, eds., TMS-AIME, Warrendale, PA, 1984, pp. 193-205.
5. C.R. Heiple and J.R. Roper: *Welding J.*, 1982, vol. 61, pp. 97s-102s.
6. C.R. Heiple, J.R. Roper, R.T. Stagner, and R.J. Aden: *Welding J.*, 1983, vol. 62, pp. 72s-77s.
7. C.R. Heiple and P. Burgardt: *Welding J.*, 1985, vol. 64, pp. 159s-162s.
8. S. Kou and Y.H. Wang: *Welding J.*, 1986, vol. 65, pp. 63s-70s.
9. S. Kou and D.K. Sun: *Metall. Trans. A*, 1985, vol. 16A, pp. 203-13.
10. M.C. Tsai and S. Kou: *Int. J. Num. Meth. Fluids*, 1989, vol. 9, pp. 1503-16.
11. T. Zacharia, A.H. Eraslan, and D.K. Aidun: *Welding J.*, 1988, vol. 67, pp. 53s-62s.
12. T. Zacharia, S.A. David, J.M. Vitek, and T. DebRoy: *Welding J.*, 1989, vol. 68, pp.499s-509s.
13. T. Zacharia, A.H. Eraslan, D.K. Aidun, and S.A. David: *Metall. Trans. B*, 1989, vol. 20B, pp. 645-59.

14. T. Zacharia, S.A. David, and J.M. Vitek: *Metall. Trans. B*, 1991, vol. 22B, pp. 233-41.
15. G.M. Oreper and J. Szekely: *J. Fluid Mech.*, 1984, vol. 147, pp. 53-79.
16. M.E. Thompson and J. Szekely: *Int. J. Heat Mass Transfer*, 1989, vol. 32, pp. 1007-19.
17. R.T.C. Choo, J. Szekely, and R.C. Welsthoff: *Welding J.*, 1990, vol. 69, pp. 346s-361s.
18. R.T.C. Choo and J. Szekely: *Welding J.*, 1992, vol. 71, pp. 77s-93s.
19. R.T.C. Choo, J. Szekely, and S.A. David: *Metall. Trans. B*, 1992, vol. 23B, pp. 371-84.
20. S.D. Kim and S.J. Na: *Welding J.*, 1992, vol. 71, pp. 179s-193s.
21. R.A. Wood and D.R. Milner: *Welding J.*, 1971, vol. 50, pp. 163s-173s.
22. B.J. Keene, K.C. Mills, J.W. Bryant, and E.D. Hondros: *Can. Metall. Q.*, 1982, vol. 21, pp. 393-403.
23. K.C. Mills and B.J. Keene: *Int. Mater. Rev.*, 1990, vol. 35, pp. 185-216.
24. P. Burgardt and R.D. Campbell: *Key Eng. Mater.*, 1992, vols. 69–70, pp. 379-416.
25. Q.Z. Diao and H.L. Tsai: *Metall. Trans. A*, 1993, vol. 24A, pp. 963-73.
26. M.C. Flemings: *Solidification Processing*, McGraw-Hill, Inc., New York, NY, 1974, pp. 244-52.
27. M.J. Voss and H.L. Tsai: *Int. J. Eng. Sci.*, 1996, vol. 34, pp. 715-37.
28. M. Choi, R. Greif, and M. Salcudean: *Num. Heat Transfer*, 1987, vol. 11, pp. 477-89.
29. P. Sahoo, T. DebRoy, and M.J. McNallan: *Metall. Trans. B*, 1988, vol. 19B, pp. 483-91.
30. S.V. Patankar: *Numerical Heat Transfer and Fluid Flow*, Hemisphere, New York, NY, 1980, pp. 96-102.
31. K.C. Chiang and H.L. Tsai: *Int. J. Heat Mass Transfer*, 1992, vol. 35, pp. 1771-78.
32. Q.Z. Diao and H.L. Tsai: *Metall. Mater. Trans. A*, 1994, vol. 25A, pp. 1051-62.
33. H.G. Kraus: *Welding J.*, 1989, vol. 68, pp. 84s-91s.
34. H.G. Kraus: *Welding J.*, 1989, vol. 68, pp. 269s-279s.
35. W.D. Bennon and F.P. Incropera: *Int. J. Heat Mass Transfer*, 1987, vol. 30, pp. 2171-87.